Rh Particles Supported on Sulfated g-C$_3$N$_4$: A Highly Efficient and Recyclable Heterogeneous Catalyst for Alkene Hydroformylation

Yukun Shi [1],*, Yang Lu [1], Tongxin Ren [1], Jie Li [1], Qiqige Hu [1], Xiaojing Hu [2], Baolin Zhu [2] and Weiping Huang [2],*

[1] Institute of Chemistry for Functionalized Materials, College of Chemistry and Chemical Engineering, Liaoning Normal University, Dalian 116029, China; NuanYY12138@163.com (Y.L.); Hollytx@163.com (T.R.); Yihan118128@163.com (J.L.); qqg0509@yeah.net (Q.H.)

[2] College of Chemistry, Nankai University, Tianjin 300071, China; hxj614@yeah.net (X.H.); zhubaolin@nankai.edu.cn (B.Z.)

* Correspondence: syk@lnnu.edu.cn (Y.S.); hwp914@nankai.edu.cn (W.H.); Tel.: +86-135-0073-1179 (Y.S.); +86-138-2009-6974 (W.H.)

Abstract: The hydroformylation of alkenes with CO and H$_2$ to manufacture aldehydes is one of the most large-scale chemical reactions. However, an efficient and recyclable heterogeneous catalyst for alkene hydroformylation is extremely in demand in academia and industry. In this study, a sulfated carbon nitride supported rhodium particle catalyst (Rh/S-g-C$_3$N$_4$) was successfully synthesized via an impregnation-borohydride reduction method and applied in the hydroformylation of alkenes. The catalysts were characterized by XRD, FTIR, SEM, TEM, XPS, and nitrogen adsorption. The influence of the sulfate content, pressure of syngas, temperature, and reaction time, as well as the stability of Rh/S-g-C$_3$N$_4$, on the hydroformylation was examined in detail. The delocalized conjugated structure in g-C$_3$N$_4$ can lead to the formation of electron-deficient aromatic intermediates with alkenes. The sulphate g-C$_3$N$_4$ has a defected surface owing to the formation of oxygen vacancies, which increased the adsorption and dispersion of RhNPs on the surface of g-C$_3$N$_4$. Therefore, Rh/S-g-C$_3$N$_4$ exhibited an outstanding catalytic performance for styrene hydroformylation (TOF = 9000 h^{-1}), the conversion of styrene could reach 99.9%, and the regioselectivity for the branched aldehyde was 52% under the optimized reaction conditions. The catalytic properties of Rh/S-g-C$_3$N$_4$ were also studied in the hydroformylation of various alkenes and displayed an excellent catalytic performance. Furthermore, the reuse of Rh/S-g-C$_3$N$_4$ was tested for five recycling processes, without an obvious decrease in the activity and selectivity under the optimum reaction conditions. These findings demonstrated that Rh/S-g-C$_3$N$_4$ is a potential catalyst for heterogeneous hydroformylation.

Keywords: g-C$_3$N$_4$; sulfated; Rh particles; hydroformylation; alkenes

1. Introduction

Hydroformylation (oxo process) has been extensively applied in industry to manufacture aldehydes by the addition of CO and H$_2$ to alkenes in one step with a 100% atom efficiency [1–3]. The aldehydes formed are valuable industrial products and intermediates in the synthesis of bulk chemicals, such as alcohols, carboxylic acids, esters, amines, and so on [4,5]. This green and clean synthetic route was accidentally found by Otto Roelen during the Fischer-Tropsch process in 1938 [6]. Today, this transformation represents one of the most large-scale reactions in industry. More than ten million tons of "oxo chemicals" are manufactured by the hydroformylation reaction [7,8].

Nowadays, commercial hydroformylation processes mainly involve homogeneous Rh-based catalysis owing to the excellent performance that can be achieved under milder reaction conditions [9,10]. However, the reuse of homogeneous Rh-based catalysts is very inconvenient. The separation of aldehydes or alcohols from homogeneous catalysts and the regeneration of expensive Rh-based catalysts are the most difficult challenges in large-scale production. To overcome these limitations of the homogeneous catalysis, various approaches for separating soluble Rh-based complex catalysts [11,12] have been developed, such as non-aqueous ionic liquids, an aqueous/organic biphasic system, supercritical carbon dioxide, a fluorous biphasic system, and supported catalysts [13–17]. Among these approaches, supported catalysts are regarded as one of the most available approaches due to their advantages of simple separation and good recycling properties [12,18–21]. In supported Rh-based catalysts, heterogeneous supported Rh particle catalysts can provide a simple but efficient method to overcome the weak point in alkene hydroformylation, and the catalytic activity of supported Rh particle catalysts is constantly lower than that of homogeneous catalysts. Therefore, the development of novel supported Rh particle catalysts with high activity and reusability remains extremely challenging and timely.

In the design of heterogeneous supported Rh particle catalysts for alkene hydroformylation, the most effective method is the selection of appropriate supports which have special properties to adjust the metal particles, such as a dispersion capability, stability, and electron effects. Two-dimensional layer-structured graphitic carbon nitride, named g-C_3N_4, possesses strong tri-s-triazine linked with tertiary amine groups in each layer, and is a suitable catalytic material in the field of photocatalysis and heterogeneous catalysis [22–24], owing to its high surface area, chemical and thermal stability, amenability to chemical modification, particular electronic structure, and low-cost preparation. Because the tri-s-triazine ring in each layer is aromatic, the 2D conjugated s-triazine prefers to form a delocalized conjugated structure like that of graphite [22,25,26]. This special conjugated structure not only interacts with double- and triple-bond reactants, such as alkenes and alkynes, but also significantly improves electron transfer in the supports, improving the stability of well-dispersed metal particles [27,28].

In particular, g-C_3N_4 has nitrogen pots with rich melon moieties, which are promising sites for adjusting its electronic structures and original properties [29,30]. Heteroatomic doping with non-metals, such as B, S, C, etc. [31–35], has formed a new series of g-C_3N_4-based catalysts with improved catalytic performances, mainly in the field of photocatalysis. Xu et al. [36] reported that sulfur-doped g-C_3N_4 displayed an outstanding photocatalytic performance for H_2 evolution under visible light with a good stability compared to that of neat g-C_3N_4, owing to the carbon being substituted by sulfur in g-C_3N_4. Parida et al. [37] reported that visible light-induced water reduction for H_2 production catalyzed by Au-sulfated g-C_3N_4 was increased by over 2.5 times compared to that of sulfated g-C_3N_4, 1.5 times compared to that of Au-g-C_3N_4, and 35 times compared to that of neat g-C_3N_4.

In this contribution, we investigate the effect of sulfate on improving the deposition of Rh particles on g-C_3N_4 and enhancing the catalytic performance of Rh/g-C_3N_4 in the hydroformylation of alkenes. The g-C_3N_4, containing rich nitrogen pots, can disperse Rh particles to form abundant catalytic active sites. Furthermore, the sulphate pre-treated procedure can not only adjust the surface functionality and electronic structure of g-C_3N_4 to improve the electron transfer and form a more stable π conjugation system, but also create a defected surface because of the formation of oxygen vacancies. This interaction strengthens the adsorption and deposition of Rh particles on the defected surface of the g-C_3N_4. Inspired by this understanding of the importance of sulfonation for the deposition of Rh particles, an assumption is proposed that the deposited Rh particles on the sulfated surface of g-C_3N_4 can exhibit an outstanding catalytic performance in styrene hydroformylation, as well as easy separation and recycling.

2. Results and Discussion

2.1. Characterization

XRD was applied to analyze the crystal phase, interlayer stacking, and structure of the synthesized g-C_3N_4. In Figure 1a, the XRD pattern of neat g-C_3N_4 demonstrates a graphitic-like layer structure, with two feature diffraction peaks at 27.4° and 13.1° (JCPDS-87-1526). The strong diffraction peak at 27.4° can be ascribed to the (002) crystal plane [23], typically representing the graphite-like characteristic interlayer stacking structure of the conjugated aromatic systems, with an interlayer distance of about 0.326 nm. The minor diffraction peak at 13.1° can be ascribed to the (100) crystal plane, representing the in-plane structural packing motif of tri-s-triazine units. The calculated lattice spacing is about 0.675 nm. Furthermore, for the X%S-g-C_3N_4, Rh/g-C_3N_4, and Rh/3%S-g-C_3N_4, no significant change of the main peaks at 13.1° and 27.4° can be observed, demonstrating that the modification of sulfur and rhodium cannot affect the crystal structure of g-C_3N_4 and the structure of tri-s-triazine is chemically stable during the structural modification. The XRD peaks of Rh do not appear in Rh/g-C_3N_4 and Rh/S-g-C_3N_4 owing to the low content and good dispersion of Rh particles.
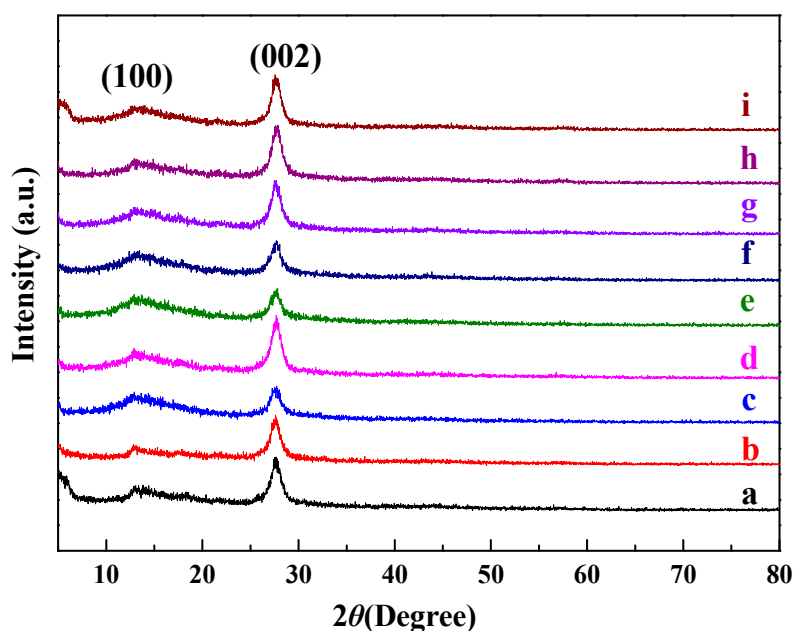
Figure 1. XRD patterns of (**a**) neat g-C_3N_4, (**b**) 1%S-g-C_3N_4, (**c**) 2%S-g-C_3N_4, (**d**) 3%S-g-C_3N_4, (**e**) 4%S-g-C_3N_4, (**f**) 5%S-g-C_3N_4, (**g**) 6%S-g-C_3N_4, (**h**) Rh/g-C_3N_4 and (**i**) Rh/3%S-g-C_3N_4.

In order to study the functional groups of neat g-C_3N_4, X%S-g-C_3N_4, Rh/g-C_3N_4 and Rh/3%S-g-C_3N_4, FTIR spectroscopy spectra were recorded and shown in Figure 2, and the spectra for all the samples are greatly similar with each other. The peak at about 812 cm^{-1} is belong to the characteristic breathing mode of tri-s-triazine rings [23], while the strong band in the range of 1200–1700 cm^{-1} with the characteristic peaks located at 1238, 1325, 1412, 1574, 1639 cm^{-1}, belongs to the characteristic stretching vibration of aromatic C-N heterocycles, and these are the typical absorption bands of triazine units. Another broad band in the range 3100–3300 cm^{-1} originates from the N-H vibration and the O-H vibration, owing to the unpolymerized amino groups and the water molecules adsorbed on the surface of g-C_3N_4. For Rh loaded g-C_3N_4 or S-g-C_3N_4, all the characteristic vibrational peaks of g-C_3N_4 are unchanged.
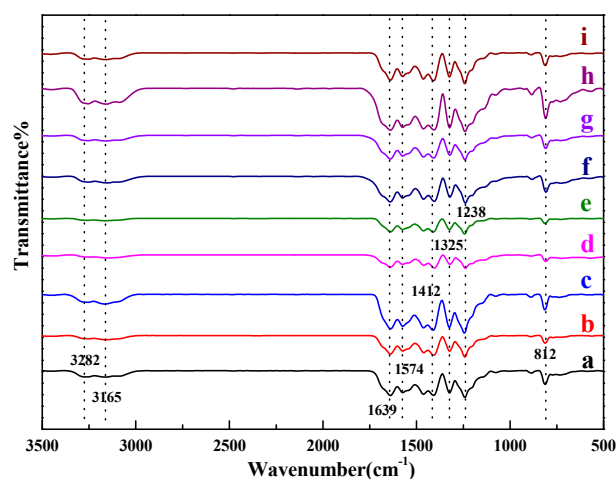
Figure 2. FTIR spectra of (**a**) neat g-C$_3$N$_4$, (**b**) 1%S-g-C$_3$N$_4$, (**c**) 2%S-g-C$_3$N$_4$, (**d**) 3%S-g-C$_3$N$_4$, (**e**) 4%S-g-C$_3$N$_4$, (**f**) 5%S-g-C$_3$N$_4$, (**g**) 6%S-g-C$_3$N$_4$, (**h**) Rh/g-C$_3$N$_4$, and (**i**) Rh/3%S-g-C$_3$N$_4$.

The morphologies and microstructural details of neat g-C$_3$N$_4$, 3%S-g-C$_3$N$_4$, and Rh/3%S-g-C$_3$N$_4$ were checked by SEM analyses in the Figure 3. Figure 3A reveals the formation of a slate-like, stacked lamellar structure in neat g-C$_3$N$_4$. The enlarged view in Figure 3B reveals that the edges of g-C$_3$N$_4$ tend to bend to decrease the surface energy. Many breakages and holes are present on the surface of the lamellar structures, owing to the release of NH$_3$ and CO$_2$ during the thermal condensation of urea. These holes produce a porous structure with a greater surface area in sulfated g-C$_3$N$_4$ samples. After sulfonation (Figure 3C), the g-C$_3$N$_4$ network decomposes and forms an irregular thin lamellar structure, resulting in an increase of the specific surface area. Simultaneously, this porous structure can also provide more growth sites for the formation of smaller-sized RhNPs. After the introduction of RhNPs on the 3%S-g-C$_3$N$_4$ (Figure 3D), the rhodium particles are uniformly dispersed on the surface of S-g-C$_3$N$_4$.
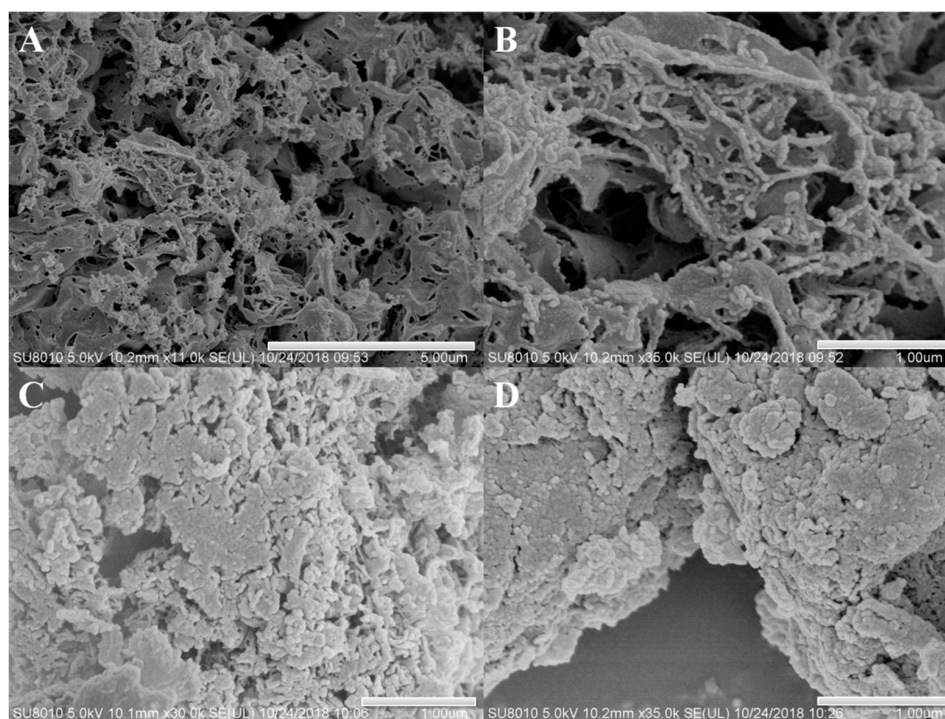
Figure 3. SEM images of g-C$_3$N$_4$ (**A**,**B**), 3%S-g-C$_3$N$_4$ (**C**), and Rh/3%S-g-C$_3$N$_4$ (**D**).

The microstructures and morphologies of Rh/g-C$_3$N$_4$ and Rh/3%S-g-C$_3$N$_4$ samples were also checked by TEM to analyze the shape, size, and distribution of RhNPs on the surface of g-C$_3$N$_4$. In Figure 4, both Rh/g-C$_3$N$_4$ and Rh/3%S-g-C$_3$N$_4$ show an obvious lamellar structure of g-C$_3$N$_4$. In Figure 4c,d, the Rh/3%S-g-C$_3$N$_4$ sample has a defected surface because of the formation of an irregular porous structure, resulting in a strengthening of the adsorption of RhNPs onto the sulphated g-C$_3$N$_4$. In addition, the uniform distribution of RhNPs on the g-C$_3$N$_4$ and S-g-C$_3$N$_4$ can be clearly observed. All of the RhNPs are strongly adhered to the surface of g-C$_3$N$_4$. Moreover, the size of Rh particles decreases more obviously in the case of S-g-C$_3$N$_4$ (2–3 nm) than that of neat g-C$_3$N$_4$ (6–7 nm), demonstrating that the sulfonation of g-C$_3$N$_4$ can efficiently improve the dispersion of RhNPs and drastically decrease the particle size of RhNPs. This demonstrates the presence of a strong interaction between the defected surface and RhNPs in sulfated g-C$_3$N$_4$ for forming smaller-sized RhNPs, which means that more Rh atoms can be provided to form catalytic active species for the hydroformylation of alkenes.
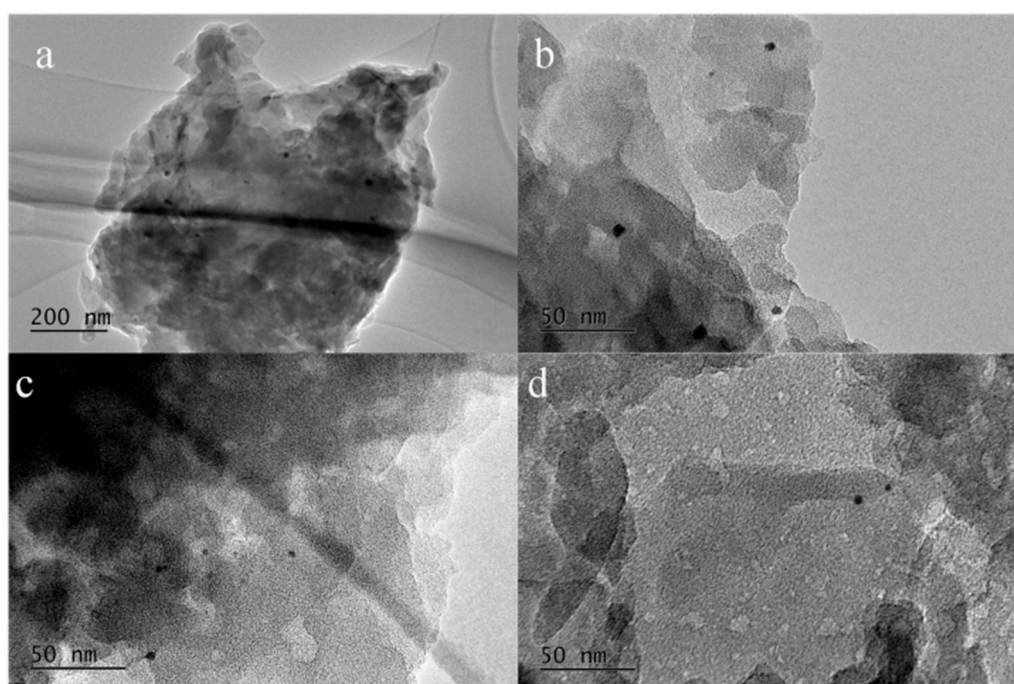
Figure 4. TEM images of Rh/g-C$_3$N$_4$ (**a,b**) and Rh/3%S-g-C$_3$N$_4$ (**c,d**).

The specific surface areas of the neat g-C$_3$N$_4$ and sulfated g-C$_3$N$_4$ are summarized in Table 1. It is obvious that the specific surface areas of all the S-g-C$_3$N$_4$ are lower than that of neat g-C$_3$N$_4$ (115.8 m^2 g^{-1}), due to the sulphate process, which results in decomposition of the g-C$_3$N$_4$ network. For the sulfated g-C$_3$N$_4$ samples, the specific surface area increases with the sulfur content from 1 to 3 wt.% and then decreases from 3 to 6 wt.% (the maximum is 78.8 m^2 g^{-1} for 3%S-g-C$_3$N$_4$). The increase of surface areas can be attributed to the sulphate process, which forms a porous structure on the layers of g-C$_3$N$_4$. However, a further increase of the sulfur content may cause the aggregation of g-C$_3$N$_4$ layers and then decrease the specific surface areas of the samples.

XPS was further applied to study the chemical composition of the Rh/3%S-g-C$_3$N$_4$ sample as shown in the Figure 5 and Figure S1. The C 1s spectrum in Figure 5a shows two peaks at binding energies of 284.6 and 287.6 eV. The peak at 284.6 eV can be attributed to the sp^2 C-C bonds of graphitic carbon adsorbed to the surface, whereas the peak at 287.6 eV corresponds to sp^3-bonded C in the N-containing aromatic ring (N-C=N) of g-C$_3$N$_4$ [38]. The N 1s peak in Figure 5b can be deconvoluted into three peaks at 398.1, 399.8, and 404.1 eV. The main peak at 398.3 eV is typically ascribed to sp^2-hybridized nitrogen (C=N-C), and the other two peaks located at 399.8 and 404.1 eV can be attributed to the

N-(C)$_3$ groups and the charging effects, respectively [39]. Figure 5c shows the XPS spectrum of Rh 3d. The strongest peak at 307.3 eV (Rh 3d$_{5/2}$), together with the peak at 312.1 eV (Rh 3d$_{3/2}$), corresponds to the metallic Rh. The binding energy at 309.1 eV is attributed to the Rh^{3+} 3d$_{5/2}$ peak, and 313.9 eV is assigned to the Rh^{3+} 3d$_{3/2}$ peak. This demonstrates that the impregnation-borohydride reduction method can effectively load RhNPs on the surface of the S-g-C$_3$N$_4$.

Table 1. Textural properties of the neat g-C$_3$N$_4$ and X%S-g-C$_3$N$_4$.

Samples	g-C$_3$N$_4$	1%S-g-C$_3$N$_4$	2%S-g-C$_3$N$_4$	3%S-g-C$_3$N$_4$	4%S-g-C$_3$N$_4$	5%S-g-C$_3$N$_4$	6%S-g-C$_3$N$_4$
S$_{BET}$ (m^2 g^{-1})	115.8	70.1	71.0	78.8	73.6	58.4	39.6
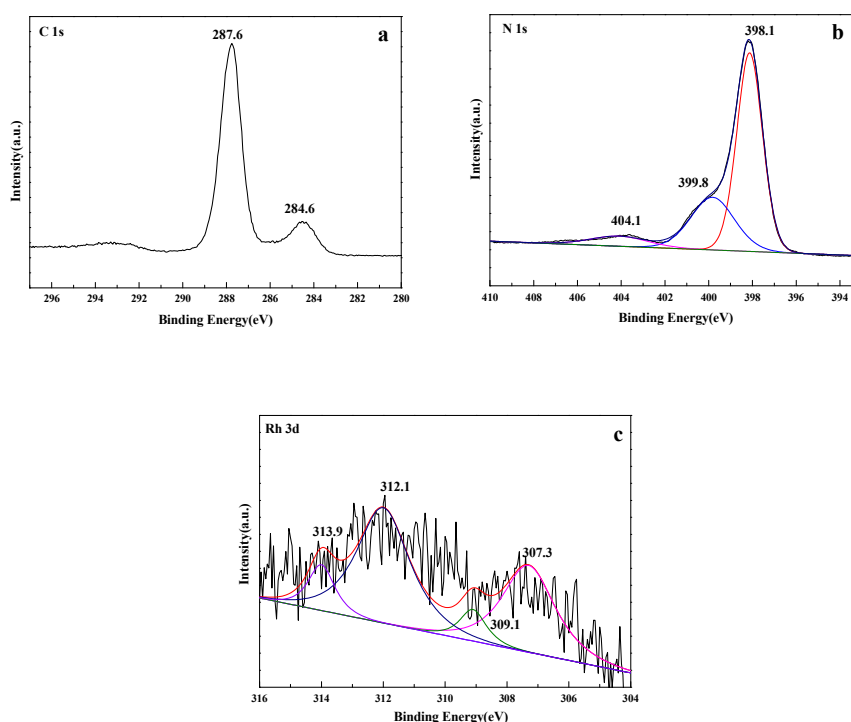
Figure 5. XPS spectra of (**a**) C 1s, (**b**) N 1s, and (**c**) Rh 3d of the Rh/3%S-g-C$_3$N$_4$ sample.

2.2. Catalytic Performance

To study the catalytic performance of Rh/S-g-C$_3$N$_4$, styrene hydroformylation was chosen as the model reaction to investigate the catalytic activity and selectivity of Rh/S-g-C$_3$N$_4$ catalysts in detail. The formed aldehydes were 3-phenylpropanal and 2-phenylpropanal, as shown in Scheme 1.
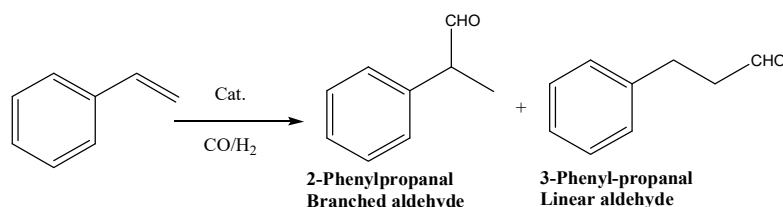
Scheme 1. Styrene hydroformylation to linear and branched aldehydes.

The obtained results illustrating the catalytic performances of Rh/g-C$_3$N$_4$ and Rh/X%S-g-C$_3$N$_4$ with different sulfur contents for styrene hydroformylation are summarized in Table 2. It can be seen that the Rh/g-C$_3$N$_4$ catalyst displays an outstanding catalytic activity for styrene hydroformylation (Entry 1, TOF = 5800 h^{-1}), due to its 2D continuous lamellar structure similar to that of graphite,

which determines its large exposed Rh active sites, high particle dispersion, and small particle size. After sulfonation, all of the Rh/X%S-g-C$_3$N$_4$ catalysts exhibit far higher activities than the Rh/g-C$_3$N$_4$ catalyst, indicating that the excellent activity of Rh/X%S-g-C$_3$N$_4$ is closely related to sulfur doping. Modifying sulfur atoms can promote the electron transfer of π-conjugated g-C$_3$N$_4$ to form a more stable π-conjugated structure, which is beneficial for forming electron-deficient aromatic intermediates with alkenes, leading to higher activity of the Rh/X%S-g-C$_3$N$_4$ catalysts. What is more important is that the S-g-C$_3$N$_4$ has a defected surface because of the formation of oxygen vacancies (confirmed by SEM and TEM), which can strengthen the adsorption of RhNPs onto the vacant oxygen sites and promote the dispersion of RhNPs to form smaller and more uniform RhNPs, resulting in more active species for styrene hydroformylation. Furthermore, the content of sulfur also plays an important role in the catalytic activities of Rh/X%S-g-C$_3$N$_4$ catalysts. The TOF increases with the sulfur content from 1 to 3 wt.% and then decreases from 3 to 6 wt.%, indicating that the optimum sulfur content should be 3 wt.%, with the highest TOF = 9000 h^{-1} (Entry 4). Rh/3%S-g-C$_3$N$_4$ represents one of the best heterogeneous catalysts for alkene hydroformylation in comparison with the reported Rh/MOF-5 [19], for which the conversion of alkene is 89.6% under the same reaction condition. The excellent catalytic performances of Rh/3%S-g-C$_3$N$_4$ could be due to the synergetic effects between S-g-C$_3$N$_4$ and RhNPs. The defected surface of S-g-C$_3$N$_4$ with a high specific surface area can also efficiently disperse RhNPs to form more small RhNPs and increase the number of active sites for the hydroformylation of alkenes. It can be obviously seen that 3%S-g-C$_3$N$_4$ has the highest SSA, and thus Rh/3%S-g-C$_3$N$_4$ has the best catalytic activity for styrene hydroformylation.

Table 2. Hydroformylation of styrene over Rh/g-C$_3$N$_4$ and Rh/S-g-C$_3$N$_4$ [a].

Entry	Catalyst	Conversion (%)	TOF (h^{-1}) [b]	Selectivity (%)	
				Aldehydes	B:L [c]
1	Rh/g-C$_3$N$_4$	64.8	5800	100	54:46
2	Rh/1%S-g-C$_3$N$_4$	87.4	7900	100	54:46
3	Rh/2%S-g-C$_3$N$_4$	96.5	8700	100	50:50
4	Rh/3%S-g-C$_3$N$_4$	99.9	9000	100	52:48
5	Rh/4%S-g-C$_3$N$_4$	93.5	8400	100	54:46
6	Rh/5%S-g-C$_3$N$_4$	82.0	7300	100	46:54
7	Rh/6%S-g-C$_3$N$_4$	77.7	7000	100	54:46

[a] Reaction conditions: Catalyst: 0.02 g; toluene: 20 mL; styrene: 1.5 mL; reaction time: 3 h; temp.: 100 °C; and syngas (CO/H$_2$ =1): 6.0 MPa. [b] TOF = number of moles of product formed/(number of moles of Rh × h). [c] B:L = 2-phenylpropanal: 3-phenylpropanal.

To study the optimized reaction conditions for styrene hydroformylation, the reaction temperature and syngas pressure were evaluated in detail. The results are shown in Table 3. In all cases, only 2-phenylpropanal and 3-phenylpropanal products can be observed, without any by-products, such as alcohols, which are derived by the hydrogenation of aldehyde products. It is well known that the conversion and aldehyde selectivity of styrene hydroformylation are strongly related to the reaction temperature. Therefore, the effect of the reaction temperature was firstly explored in the range of 80–100 °C, and a good conversion of 99.9% styrene, with an excellent TOF of 9000 h^{-1}, was achieved at 100 °C. Therefore, the optimum reaction temperature is near 100 °C. Although the conversion of styrene increases with a rising reaction temperature, the selectivity to 2-phenylpropanal decreases obviously from 73% to 53%, indicating that a high temperature is beneficial for the formation of 3-phenylpropanal. The total pressure of syngas (CO/H$_2$ = 1) is also a key factor in styrene hydroformylation. As shown in Table 3 (entries 3–5), the pressure of syngas has less impact on the selectivity of products, but an enhanced pressure from 4.0 to 6.0 MPa drastically increases the conversion of styrene from 64.9% to 99.9% at the same reaction temperature. Therefore, the optimum reaction conditions (100 °C and 6.0 MPa CO/H$_2$) were chosen through systematic investigations for the following studies.

Table 3. Optimization of hydroformylation of styrene over Rh/3%S-g-C$_3$N$_4$ [a].

Entry	Temperature (°C)	Pressure (MPa)	Conversion (%)	TOF (h^{-1}) [b]	Selectivity (%)	
					Aldehydes	B:L [c]
1	80	6.0	18.4	1700	100	73:27
2	90	6.0	56.1	5100	100	65:35
3	100	6.0	99.9	9000	100	53:47
4	100	5.0	91.8	8300	100	51:49
5	100	4.0	64.9	5900	100	48:52

[a] Reaction conditions: Rh/3%S-g-C$_3$N$_4$: 0.02 g; toluene: 20 mL; styrene: 1.5 mL; reaction time: 3 h; and CO:H$_2$ = 1.
[b] TOF = number of moles of product formed/(number of moles of Rh × h). [c] B:L = 2-phenylpropanal: 3-phenylpropanal.

Figure 6 reveals the conversion and selectivity for branched aldehyde change with the reaction time. It is obvious that the styrene conversion increases with increases in the reaction time and reaches the maximum conversion at 3 h. Therefore, the optimum conditions, corresponding to the maximum styrene conversion (99.9%), were found to be 100 °C catalyzed by Rh/3%S-g-C$_3$N$_4$ under 6.0 MPa syngas (CO/H$_2$ = 1) for 3 h. In the primary stage of the reaction, the selectivity of branched aldehyde (2-phenylpropanal) is 67.0%, indicating that the formation of 2-phenylpropanal is the main reaction process of styrene hydroformylation. This can be attributed to the α-carbon of styrene, which favors the attraction of Rh metal to form a stable rhodium α-arylalkyl intermediate, resulting in a high selectivity for branched aldehyde [40]. However, as the reaction proceeds, hydroformylation generating 3-phenylpropanal dominates the reaction process, which therefore decreases the selectivity of 2-phenylpropanal in theproducts.
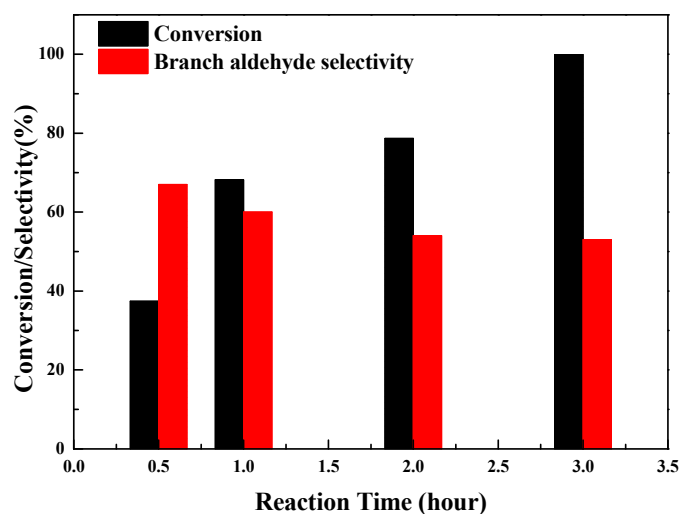
Figure 6. Effect of reaction time on conversion and selectivity for branched aldehyde over Rh/3%S-g-C$_3$N$_4$.

To investigate the scope of alkene hydroformylation, the Rh/3%S-g-C$_3$N$_4$ catalyst was further applied in the hydroformylation of various alkenes under the optimum reaction conditions, as shown in Table 4. It is obvious that the various alkenes are all hydroformylated, with outstanding catalytic performances. In the hydroformylation of linear alkenes (entries 2 and 3), the conversion decreases with the increased chain length of alkenes, demonstrating that the coordination of alkenes to Rh in the catalytic process becomes more difficult with the increase in the chain length of alkenes. It is worth noting that Rh/3%S-g-C$_3$N$_4$ is not effective and highly regioselective, producing linear aldehydes from these alkenes (entries 1–3). The α-carbon of styrene prefers to attack the electropositive Rh metal to form a stable rhodium α-arylalkyl intermediate, resulting in a higher selectivity for branched aldehyde. For linear alkenes such as 1-hexene and 1-octene, the high selectivity of branched aldehyde may be

due to the isomerization of terminal alkene to isomerized alkene, which can also be hydroformylated into branched aldehydes.

Table 4. Hydroformylation of various alkenes over Rh/3%S-g-C$_3$N$_4$ [a].

Entry	Substrates	Conversion (%)	TOF (h^{-1}) [b]	Selectivity (%)	
				Aldehydes	B:L [c]
1	styrene	99.9	9000	100	53:47
2	1-hexene	97.1	8000	99.7	56:44
3	1-octene	94.9	6300	97.9	57:43
4	cyclohexene	62.9	6400	100	-

[a] Reaction conditions: Rh/3%S-g-C$_3$N$_4$: 0.02 g; toluene: 20 mL; substrates: 1.5 mL; reaction time: 3 h; temp.: 100 °C; and syngas (CO/H$_2$ = 1): 6.0 MPa. [b] TOF = number of moles of product formed/(number of moles of Rh × h). [c] B:L = branched aldehyde: linear aldehyde.

The cyclic stability is an important factor in the use of heterogeneous catalysts, so the cyclic experiments of Rh/3%S-g-C$_3$N$_4$ were evaluated for five recycling processes, as shown in Figure 7. After the reaction, Rh/3%S-g-C$_3$N$_4$ was easily separated through filtering and directly reused in the next cyclic experiment. As shown in Figure 7, Rh/3%S-g-C$_3$N$_4$ can be reused after being recycled five times, without a decrease in catalytic activity and selectivity, demonstrating that Rh/3%S-g-C$_3$N$_4$ is a stable catalyst for alkene hydroformylation. The stability of Rh/3%S-g-C$_3$N$_4$ may be due to the defected surface of S-g-C$_3$N$_4$, which can be beneficial for the adsorption and dispersion of RhNPs onto the surface of S-g-C$_3$N$_4$.
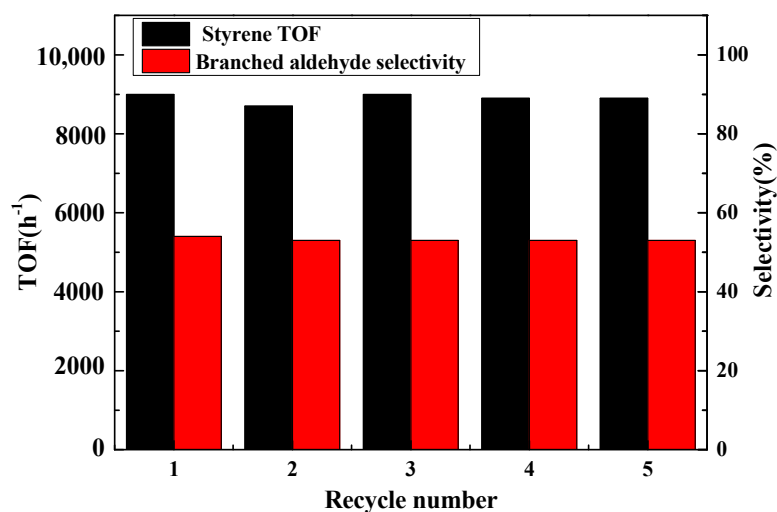
Figure 7. Cyclic stability of the Rh/3%S-g-C$_3$N$_4$ catalyst for styrene hydroformylation.

3. Materials and Methods

All of the chemical reagents were purchased with an analytical grade and used without further purification. Urea and toluene were purchased from the Sinopharm Chemical Reagent Co., Ltd., Shanghai, China. Various alkenes were purchased from the Energy Chemical Company. RhCl$_3$ was purchased from Shaanxi Kaida Chemical Engineering Co. Ltd., Baoji, China.

3.1. Preparation of Neat g-C$_3$N$_4$

G-C$_3$N$_4$ was prepared from urea via the facile template-free method, as reported in our previous work [41].

3.2. Preparation of Sulfated g-C₃N₄

The as-prepared 0.5 g g-C$_3$N$_4$ was dispersed in 20 mL distilled water. After low-energy sonication for 0.5 h, a calculated amount of H$_2$SO$_4$ (6 M) was added and vigorously stirred for another 6 h at 60 °C to form slurry, which was then dried in an oven at 80 °C. The obtained solid was calcined at 400 °C for 2 h in a muffle furnace to remove any impurities. By adding different calculated amounts of H$_2$SO$_4$ (6 M), 1, 2, 3, 4, 5, and 6 wt.% sulfated g-C$_3$N$_4$ samples were prepared and marked as X%S-g-C$_3$N$_4$, where X was the calculated weight percent of S in the samples.

3.3. Preparation of the Sulfated g-C₃N₄ Supported Rh Particle Catalyst

The S-g-C$_3$N$_4$ supported Rh particle catalyst (Rh/X%S-g-C$_3$N$_4$) was prepared via an impregnation-chemical reducing process. The preparation process of the Rh/S-g-C$_3$N$_4$ catalysts is shown in Scheme 2.
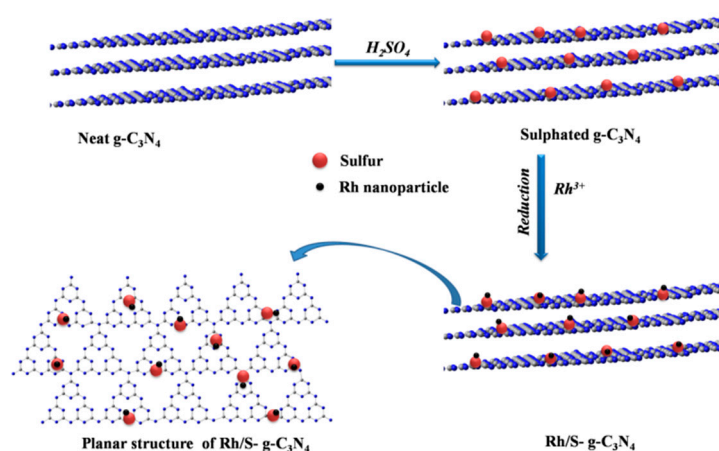
Scheme 2. Illustration of the preparation process of sulfated carbon nitride supported rhodium particle (Rh/S-g-C$_3$N$_4$) catalysts.

Typically, 0.3 g X%S-g-C$_3$N$_4$ was dispersed into 6 mL RhCl$_3$ (2.47 M) aqueous solution and stirred for 24 h. After 2 h low-energy sonication, the mixture was centrifuged and transferred into a 100 mL flask. Next, 10 mL fresh NaBH$_4$ aqueous solution (17.76 M) was added dropwise with stirring into the mixture in an ice-water bath. After the addition of NaBH$_4$, the mixture was continually stirred for another 1 h at 0 °C and room temperature, respectively. The solid was repeatedly centrifuged and washed to neutral with distilled water, and finally washed three times with ethanol. The product was dried at 40 °C for 12 h in vacuum. For a comparative study, Rh/g-C$_3$N$_4$ was prepared using a similar method, without sulphate treatment. The Rh loading of all the catalysts used in the present study was measured by ICP-AES; the content of Rh was 0.25 wt.%.

3.4. Sample Characterization

The morphologies and microstructures of the synthesized samples were examined by TEM (JEM-2100F, Jeol, Akishima, Japan) and SEM (SS-550, Shimadzu, Shimadzu, Japan).The chemical states of Rh in catalysts were analyzed by XPS (Escalab 250Xi, Thermo Fisher Scientific, Waltham, MA, USA), and the binding energies of all the elements were calibrated using C 1s (E$_b$ = 284.6 eV) as the reference. The phase structures of samples were determined by XRD (D8 advance, Bruker, Germany) with Cu Ka radiation (λ = 1.54 Å). The 2θ scanning range was recorded from 5° to 80° with a scanning rate of 2°min^{-1}. The Rh contents of samples were measured by ICP-AES (ICAP-Qc, Thermo Fisher Scientific, Waltham, MA, USA). Textural characterization of samples was checked by N$_2$ adsorption (ASIQM0000-4, Quantachrome, Boynton Beach, FL, USA) from 1.0×10^{-5} to 0.995 P/P$_0$. Before the measurement, the samples were degassed at 150 °C for 12 h.

3.5. Catalytic Activity Test

Alkene hydroformylation was carried out in a 60 mL stainless steel autoclave reactor with a magnetic stirrer. Typically, the required amounts of catalyst, solvent, and alkene were placed in the autoclave reactor. The reactor was sealed and purged three times with syngas, and subsequently pressurized to the required pressure, before being heated to the reaction temperature and maintained for the time under stirring. After the desired reaction time, the reaction was stopped and the sample was cooled to room temperature and depressurized. The reaction mixtures were withdrawn for GC analysis (GC-7900 A, Lianzhong Analytical Instrument Co., Ltd., Zaozhuang, China) equipped with a flame ionization detector and a 30 m × 0.32 mm × 0.33 μm SE-54 column. The temperature of the injection point and FID detector was 240 and 250 °C, respectively.

4. Conclusions

In this study, sulphated g-C_3N_4 supported rhodium particle catalysts were synthesized via an impregnation-borohydride reduction method and exhibited outstanding catalytic performances for styrene hydroformylation (TOF = 9000 h^{-1}), due to the delocalized conjugated π structure of g-C_3N_4, which can form electron-deficient aromatic intermediates with alkenes. Compared with Rh/g-C_3N_4, the outstanding catalytic performances of Rh/S-g-C_3N_4 can be ascribed to the defected surface of S-g-C_3N_4, which can be beneficial for the adsorption and dispersion of RhNPs onto the surface of g-C_3N_4. Moreover, Rh/S-g-C_3N_4 exhibits outstanding catalytic performances for different alkene hydroformylation with a good selectivity to formed aldehydes. What is more important is that Rh/S-g-C_3N_4 can be easily separated and directly reused in the next cyclic experiment, without an obvious loss in catalytic activity and selectivity after five recycling processes. In summary, a sulphated g-C_3N_4 supported rhodium particle seems to be a promising catalyst for styrene hydroformylation.

Supplementary Materials: The following are available online at http://www.mdpi.com/2073-4344/10/11/1359/s1: Figure S1: XPS spectra of survey (A) and S 2p core levels (B) for Rh/3%S-g-C_3N_4 and Table S1: Effect of the reaction medium on Rh/3%S-g-C_3N_4 catalyzed hydroformylation.

Author Contributions: Y.L. performed the experiments and wrote the original draft; T.R., J.L., Q.H. and X.H. conducted data processing; Y.S., B.Z. and W.H. conceived the concept. All the authors contributed to the writing of the manuscript. All authors have read and agreed to the published version of the manuscript.

Conflicts of Interest: The authors declare no conflict of interest.

References

1. Hebrard, F.; Kalck, P. Cobalt-catalyzed hydroformylation of alkenes: Generation and recycling of the carbonyl species, and catalytic cycle. *Chem. Rev.* **2009**, *109*, 4272–4282. [CrossRef]
2. Franke, R.; Selent, D.; Borner, A. Applied hydroformylation. *Chem. Rev.* **2012**, *112*, 5675–5732. [CrossRef]
3. Piras, I.; Jennerjahn, R.; Jackstell, R.; Spannenberg, A.; Franke, R.; Beller, M. A general and efficient Iridium-catalyzed hydroformylation of olefins. *Angew. Chem.* **2011**, *123*, 294–298. [CrossRef]
4. Tao, L.; Zhong, M.M.; Chen, J.; Jayakumar, S.J.; Liu, L.N.; Li, H.; Yang, Q.H. Heterogeneous hydroformylation of long-chain alkenes in IL-in-oil Pickering emulsion. *Green Chem.* **2018**, *20*, 188–196. [CrossRef]
5. Li, C.Y.; Yan, L.; Lu, L.L.; Xiong, K.; Wang, W.L.; Jiang, M.; Liu, J.; Song, X.G.; Zhan, Z.P.; Jiang, Z.; et al. Single atom dispersed Rh-biphephos&PPh3@porous organic copolymers: Highly efficient catalysts for continuous fixed-bed hydroformylation of propene. *Green Chem.* **2016**, *18*, 2995–3005.
6. Dong, K.W.; Fang, X.J.; Jackstell, R.; Beller, M. A novel Rhodium-catalyzed domino-hydroformylation-reaction for the synthesis of sulphonamides. *Chem. Commun.* **2015**, *51*, 5059–5062. [CrossRef]
7. Jagtap, S.A.; Bhanage, B.M. Rhodium/phosphine catalysed selective hydroformylation of biorenewable olefins. *Appl. Organomet. Chem.* **2018**, *32*, 4478–4486. [CrossRef]

8. Schmitz, C.; Holthusen, K.; Leitner, W.; Franciò, G. Highly regio- and enantioselective hydroformylation of vinyl esters using bidentate phosphine, P-chiral phosphorodiamidite ligands. *ACS Catal.* **2016**, *6*, 1584–1589. [CrossRef]

9. Makhubela, B.C.E.; Jardine, A.; Smith, G.S. Rh(I) complexes supported on a biopolymer as recyclable and selective hydroformylation catalysts. *Green Chem.* **2012**, *14*, 338–347. [CrossRef]

10. Sun, Q.; Dai, Z.F.; Liu, X.L.; Sheng, N.; Deng, F.; Meng, X.J.; Xiao, F.S. Highly efficient heterogeneous hydroformylation over Rh-metalated porous organic polymers: Synergistic effect of high ligand concentration and flexible framework. *J. Am. Chem. Soc.* **2015**, *137*, 5204–5209. [CrossRef]

11. Zhao, Y.P.; Zhang, X.M.; Sanjeevi, J.; Yang, Q.H. Hydroformylation of 1-octene in Pickering emulsion constructed by amphiphilic mesoporous silica particles. *J. Catal.* **2016**, *334*, 52–59. [CrossRef]

12. Hou, C.; Zhao, G.F.; Ji, Y.J.; Niu, Z.Q.; Wang, D.S.; Li, Y.D. Hydroformylation of alkenes over Rhodium supported on the metal-organic framework ZIF-8. *Nano Res.* **2014**, *79*, 1364–1369. [CrossRef]

13. Peral, D.; Stehl, D.; Bibouche, B.; Yu, H.; Mardoukh, J.; Schomäcker, R.; Klitzing, R.V.; Vogt, D. Colloidal polymer particles as catalyst carriers and phase transfer agents in multiphasic hydroformylation reactions. *J. Colloid Interface Sci.* **2018**, *513*, 638–646. [CrossRef] [PubMed]

14. Wang, Y.Q.; Yan, L.; Li, C.Y.; Jiang, M.; Wang, W.L.; Ding, Y.J. Highly efficient porous organic copolymer supported Rh catalysts for heterogeneous hydroformylation of butenes. *Appl. Catal. A Gen.* **2018**, *551*, 98–105. [CrossRef]

15. Chuai, H.Y.; Su, P.H.; Liu, H.C.; Zhu, B.L.; Zhang, S.M.; Huang, W.P. Alkali and alkaline earth cation-decorated TiO$_2$ nanotube-supported Rh catalysts for vinyl acetate hydroformylation. *Catalysts* **2019**, *9*, 194. [CrossRef]

16. Su, P.H.; Liu, X.T.; Chen, Y.; Liu, H.C.; Zhu, B.L.; Zhang, S.M.; Huang, W.P. Synthesis and characterization of Rh/B-TNTs as a recyclable catalyst for hydroformylation of olefin containing -CN functional group. *Nanomaterials* **2018**, *8*, 755. [CrossRef]

17. Gorbunov, D.; Safronova, D.; Kardasheva, Y.; Maximov, A.; Rosenbergand, E.; Karakhanov, E. New heterogeneous Rh-containing catalysts immobilized on a hybrid organic-inorganic surface for hydroformylation of unsaturated compounds. *ACS Appl. Mater. Interfaces* **2018**, *10*, 26566–26575. [CrossRef]

18. Tan, M.H.; Ishikuro, Y.; Hosoi, Y.; Yamane, N.; Ai, P.P.; Zhang, P.P.; Yang, G.H.; Wu, M.B.; Yang, R.Q.; Tsubaki, N. PPh$_3$ functionalized Rh/rGO catalyst for heterogeneous hydroformylation: Bifunctional reduction of graphene oxide by organic ligand. *Chem. Eng. J.* **2017**, *330*, 863–869. [CrossRef]

19. Vu, T.V.; Kosslick, H.; Schulz, A.; Harloff, J.; Paetzold, E.; Lund, H.; Kragl, U.; Schneider, M.; Fulda, G. Influence of the textural properties of Rh/MOF-5 on the catalytic properties in the hydroformylation of olefins. *Microporous Mesoporous Mater.* **2012**, *154*, 100–106. [CrossRef]

20. Shi, Y.K.; Hu, X.J.; Chen, L.; Lu, Y.; Zhu, B.L.; Zhang, S.M.; Huang, W.P. Boron modified TiO$_2$ nanotubes supported Rh-nanoparticle catalysts for highly efficient hydroformylation of styrene. *New J. Chem.* **2017**, *41*, 6120–6126. [CrossRef]

21. Shi, Y.K.; Hu, X.J.; Zhu, B.L.; Wang, S.R.; Zhang, S.M.; Huang, W.P. Synthesis and characterization of TiO$_2$ nanotube supported Rh-nanoparticle catalysts for regioselective hydroformylation of vinyl acetate. *RSC Adv.* **2014**, *4*, 62215–62222. [CrossRef]

22. Wang, Y.; Wang, X.C.; Antonietti, M. Polymeric graphitic carbon nitride as a heterogeneous organocatalyst: From photochemistry to multipurpose catalysis to sustainable chemistry. *Angew. Chem. Int. Ed.* **2012**, *51*, 68–89. [CrossRef] [PubMed]

23. Xu, M.; Han, L.; Dong, S.J. Facile fabrication of highly efficient g-C$_3$N$_4$/Ag$_2$O heterostructured photocatalysts with enhanced visible-light photocatalytic activity. *ACS Appl. Mater. Interf.* **2013**, *5*, 12533–12540. [CrossRef] [PubMed]

24. Singh, J.A.; Overbury, S.H.; Dudney, N.J.; Liand, M.J.; Veith, G.M. Gold particles supported on carbon nitride: Influence of surface hydroxyls on low temperature carbon monoxide oxidation. *ACS Catal.* **2012**, *2*, 1138–1146. [CrossRef]

25. Dong, G.H.; Zhao, K.; Zhang, L.Z. Carbon self-doping induced high electronic conductivity and photoreactivity of g-C$_3$N$_4$. *Chem. Commun.* **2012**, *48*, 6178–6180. [CrossRef] [PubMed]

26. Zhang, J.Y.; Wang, Y.H.; Jin, J.; Zhang, J.; Lin, Z.; Huang, F.; Yu, J.G. Efficient visible-light photocatalytic hydrogen evolution and enhanced photostability of core/shell CdS/g-C$_3$N$_4$ nanowires. *ACS Appl. Mater. Interfaces* **2013**, *5*, 10317–10324. [CrossRef] [PubMed]

27. Zhang, W.Y.; Huang, H.J.; Li, F.; Deng, K.M.; Wang, X. Palladium particles supported on graphitic carbon nitride-modified reduced graphene oxide as highly efficient catalysts for formic acid and methanol electrooxidation. *J. Mater. Chem. A* **2014**, *2*, 19084–19094. [CrossRef]

28. Wang, Q.J.; Che, J.G. Origins of distinctly different behaviors of Pd and Pt contacts on graphene. *Phys. Rev. Lett.* **2009**, *103*, 66802–66805. [CrossRef]

29. Liu, Q.; Zhang, J.Y. Graphene supported Co-g-C_3N_4 as a novel metal-macrocyclic electrocatalyst for the oxygen reduction reaction in fuel cells. *Langmuir* **2013**, *29*, 3821–3828. [CrossRef]

30. Zhang, H.P.; Du, A.J.; Gandhi, N.S.; Jiao, Y.; Zhang, Y.P.; Lin, X.Y.; Lu, X.; Tang, Y.H. Metal-doped graphitic carbon nitride (g-C_3N_4) as selective NO_2 sensors: A first-principles study. *Appl. Surf. Sci.* **2018**, *455*, 1116–1122. [CrossRef]

31. Liu, G.; Niu, P.; Sun, C.H.; Smith, S.C.; Chen, Z.G.; Lu, G.Q.; Cheng, H.M. Unique electronic structure induced high photoreactivity of sulfur-doped graphitic C_3N_4. *J. Am. Chem. Soc.* **2010**, *132*, 11642–11648. [CrossRef] [PubMed]

32. Wang, Y.; Li, H.R.; Yao, J.; Wang, X.C.; Antonietti, M. Synthesis of boron doped polymeric carbon nitride solids and their use as metal-free catalysts for aliphatic C-H bond oxidation. *Chem. Sci.* **2011**, *2*, 446–450. [CrossRef]

33. Raziq, F.; Humayun, M.; Ali, A.; Wang, T.T.; Khan, A.; Fu, Q.Y.; Luo, W.; Zeng, H.P.; Zheng, Z.P.; Khan, B.; et al. Synthesis of S-doped porous g-C_3N_4 by using ionic liquids and subsequently coupled with Au-TiO_2 for exceptional cocatalyst-free visible-light catalytic activities. *Appl. Catal. B Environ.* **2018**, *237*, 1082–1090. [CrossRef]

34. Zou, J.Y.; Yu, Y.Z.; Yan, W.J.; Meng, J.; Zhang, S.C.; Wang, J.G. A facile route to synthesize boron-doped g-C_3N_4 nanosheets with enhanced visible-light photocatalytic activity. *J. Mater. Sci.* **2019**, *54*, 6867–6881. [CrossRef]

35. Jiang, G.G.; Cao, J.W.; Chen, M.; Zhang, X.M.; Dong, F. Photocatalytic NO oxidation on N-doped TiO_2/g-C_3N_4 heterojunction: Enhanced efficiency, mechanism and reaction pathway. *Appl. Surf. Sci.* **2018**, *458*, 77–85. [CrossRef]

36. Hong, J.D.; Xia, X.Y.; Wang, Y.S.; Xu, R. Mesoporous carbon nitride with in situ sulfur doping for enhanced photocatalytic hydrogen evolution from water under visible light. *J. Mater. Chem.* **2012**, *22*, 15006–15012. [CrossRef]

37. Patnaik, S.; Martha, S.; Madras, G.; Parida, K. The effect of sulfate pre-treatment to improve the deposition of Au-particles in a gold-modified sulfated g-C_3N_4 plasmonic photocatalyst towards visible light induced water reduction reaction. *Phys. Chem. Chem. Phys.* **2016**, *18*, 28502–28514. [CrossRef]

38. Ge, L.; Zuo, F.; Liu, J.K.; Ma, Q.; Wang, C.; Sun, D.Z.; Bartels, L.; Feng, P.Y. Synthesis and efficient visible light photocatalytic hydrogen evolution of polymeric g-C_3N_4 coupled with CdS quantum dots. *J. Phys. Chem. C* **2012**, *116*, 13708–13714. [CrossRef]

39. Sun, C.Z.; Zhang, H.; Liu, H.; Zheng, X.X.; Zou, W.X.; Dong, L.; Qi, L. Enhanced activity of visible-light photocatalytic H_2 evolution of sulfur-doped g-C_3N_4 photocatalyst via nanoparticle metal Ni as cocatalyst. *Appl. Catal. B Environ.* **2018**, *235*, 66–74. [CrossRef]

40. Dydio, P.; Reek, J.N.H. Supramolecular control of selectivity in hydroformylation of vinyl arenes: Easy access to valuable β-aldehyde intermediates. *Angew. Chem. Int. Ed.* **2013**, *52*, 3878–3882. [CrossRef]

41. Shi, Y.K.; Hu, X.J.; Zhao, J.T.; Zhou, X.J.; Zhu, B.L.; Zhang, S.M.; Huang, W.P. CO oxidation over Cu_2O deposited on 2D continuous lamellar g-C_3N_4. *New J. Chem.* **2015**, *39*, 6642–6648. [CrossRef]